

A CMOS Magnetoresistive Sensor Front-End With Mismatch-Tolerance and Sub-ppm Sensitivity for Magnetic Immunoassays

Xiahao Zhou^{1b}, Student Member, IEEE, Michael Sveiven, and Drew A. Hall^{1b}, Senior Member, IEEE

Abstract—Magnetic biosensing is an emerging technique for ultra-sensitive point-of-care (PoC) biomolecular detection. However, the large baseline-to-signal ratio and sensor-to-sensor mismatch in magnetoresistive (MR) biosensors severely complicates the design of the analog front-end (AFE) due to the high dynamic range (DR) required. The proposed AFE addresses these issues through new architectural and circuit level techniques including fast settling duty-cycle resistors (DCRs) to reduce readout time and a high frequency interference rejection (HFIR) sampling technique embedded in the ADC to relax the DR requirement. The AFE achieves an input-referred noise of 46.4 nT/ $\sqrt{\text{Hz}}$, an input-referred baseline of less than 0.235 mT, and a readout time of 11 ms while consuming just 1.39 mW. Implemented in a 0.18 μm CMOS process, this work has state-of-the-art performance with 22.7 \times faster readout time, >7.8 \times lower baseline, and 2.3 \times lower power than previously reported MR sensor AFEs.

Index Terms—Magnetic immunoassay, magnetoresistive sensor, sensor analog front-end, sensor mismatch.

I. INTRODUCTION

POINT-OF-CARE (PoC) biomolecular testing has drawn considerable attention worldwide due to its convenience, portability, and potential for long-term disease surveillance [1], [2]. While conventional *in-vitro* diagnostic techniques rely on bulky and expensive medical instrumentation (mostly optical-based) located in centralized facilities, the push towards PoC devices has focused on moving these devices out of the lab and into the field (*e.g.*, clinics, bedside, at-home, etc.). Thus, there has been significant interest in miniaturization and reducing turnaround time, ideally without compromising assay performance (*i.e.* sensitivity and specificity) [3]. Such advances could lead to broader access and a democratization of healthcare, particularly in developing parts of the world where such biomolecular testing infrastructure currently does not exist [4], [5].

Manuscript received July 19, 2019; revised September 12, 2019; accepted October 10, 2019. Date of publication October 25, 2019; date of current version December 31, 2019. This work was supported by the National Science Foundation under Grant ECCS-1454608 and Qualcomm. This paper was recommended by Associate Editor M. Ghovanloo. (Corresponding author: Drew A. Hall.)

The authors are with the Department of Electrical and Computer Engineering, University of California, San Diego, La Jolla, CA 92093 USA (e-mail: xiz250@ucsd.edu; msveiven@eng.ucsd.edu; drewhall@ucsd.edu).

Color versions of one or more of the figures in this article are available online at <http://ieeexplore.ieee.org>.

Digital Object Identifier 10.1109/TBCAS.2019.2949725

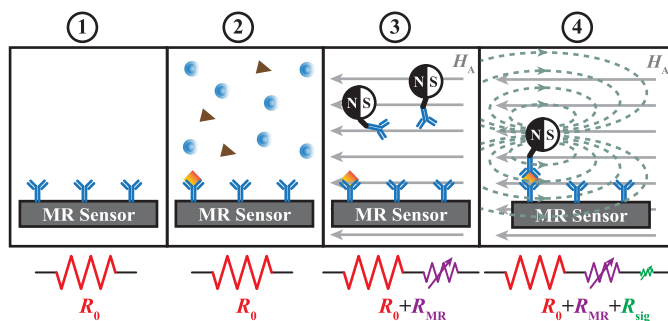


Fig. 1. Illustration of a magnetic immunoassay where underlying magnetic sensors detect magnetic nanoparticle labeled antigen-antibody complexes.

Optical- and electrochemical-based PoC biosensors are the most prevalent today [6]–[8]. Optical biosensors including colorimetric [9], fluorescent [10], and plasmonic [11] have been reported to cover a wide range of sensitivity and portability. These are often smaller versions of their laboratory equivalent, albeit with sacrifices in performance and robustness due to compromises made for portability. Electrochemical sensors are also very common, largely due to the glucometer [12], but have failed to be as successful for other diseases to date. One issue with both optical and electrochemical biosensors is their cross-sensitivity to other constituents in the assay such as the sample matrix (*e.g.*, pH, temperature, salinity, turbidity, etc.) and high abundance biomolecules (*e.g.*, albumin, globulin, fibrinogen, etc.). While sample preparation techniques can mitigate these issues in well-equipped, centralized laboratories, they are exceptionally hard to perform reproducibly in a PoC setting.

Magnetic sensors, often found today in hard disk drives and magnetic random-access memories, have shown great promise as biosensors [13]–[21], partly because the transduction mechanism is orthogonal to the sample matrix [22]. This allows very high sensitivity measurements with no magnetic background signal [23]. This contrasts with optical assays, which are sensitive to label bleaching and autofluorescence [24], [25] and electrochemical assays that are sensitive to Debye screening, pH, and other redox active molecules [26].

To use magnetic sensors for *in-vitro* assays, a modified version of the classical analytical enzyme-linked immunosorbent assay (ELISA) is needed. As shown in Fig. 1, a magnetic immunoassay (MIA) consists of the following steps: 1) Capture antibodies are

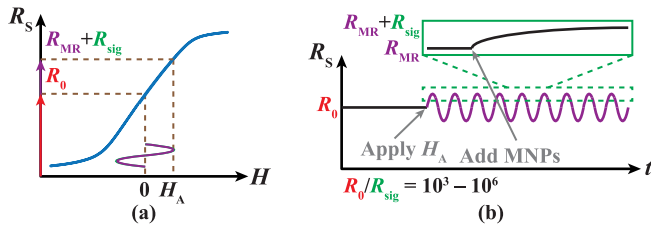


Fig. 2. (a) Illustration of a magnetoresistive sensor transfer curve and (b) magnetoresistive sensor response in a MIA with a sinusoidal H_A .

immobilized on the sensor surface using one of several different surface chemistries [27]–[30]. 2) The biological sample (*e.g.*, blood, urine, saliva, etc.) is added and the capture antibodies selectively bind to the antigen of interest providing the assay specificity. 3) The unbound sample is washed away and magnetic nanoparticle (MNP) labeled detection antibodies are added. These antibodies bind to the target antigen to form a sandwich-like structure around the target antigen. 4) Lastly, a magnetic field, H_A , is applied that magnetizes the superparamagnetic MNPs. The underlying magnetic sensor detects the stray field to quantify the number of captured antigens.

Several magnetic sensors have been demonstrated for such biosensing applications, including Hall effect [17], [18], giant magnetoresistive (GMR) [19]–[21], and tunneling magnetoresistive (TMR) [31]. Fig. 2(a) illustrates the response of a magnetoresistive (MR) sensor to a magnetic field where the linear portion of the curve is used for sensing. The magnetoresistance, R_{MR} , transduces the magnetic field into electrical resistance through spin-dependent scattering or tunneling for GMR and TMR devices, respectively [32], [33]. Thus, the resistance is proportional to the magnetic field sensed by the sensor. GMR spin-valve sensors were selected for this work due to their high sensitivity [34]. Although TMR sensors have higher MR ratios ($\sim 100\%$ vs. $\sim 10\%$ for GMR), they suffer from much worse $1/f$ noise ($1/f$ corner frequency of ~ 1 MHz vs. ~ 1 kHz for GMR) resulting in lower SNR and are harder to fabricate [35], [36].

In the context of the MIA, as MNPs become tethered to the sensor surface through binding events [37], the resistance increases from R_0 (with $H_A = 0$) to $R_0 + R_{MR} + R_{sig}$ following Langmuir binding kinetics where R_{sig} is the resistance change due to the stray field of the MNPs and thus proportional to the number of captured antigen [Fig. 2(b)]. Unfortunately, the tethered MNPs generate an incredibly small R_{sig} ($\mu\Omega - m\Omega$) that is on top of R_{MR} ($1 - 100 \Omega$) and R_0 ($0.1 - 5 k\Omega$). Thus, R_{sig} is often $10^3 - 10^6 \times$ smaller than R_0 . This makes the readout circuit design challenging since it requires an analog front-end (AFE) with more than 120 dB of dynamic range (DR). While a reference sensor can be used to reject common-mode signals such as the R_0 and R_{MR} baselines, this technique is ultimately limited by the sensor mismatch, in both R_0 and R_{MR} . GMR sensor arrays have 5–10% mismatch, even intra-chip, due to fabrication challenges around the uniformity of the thin film stack [38].

To address this, we propose a CMOS architecture for GMR sensor arrays that is tolerant of up to 10% sensor mismatch. The resulting AFE and ADC achieves state-of-the-art performance

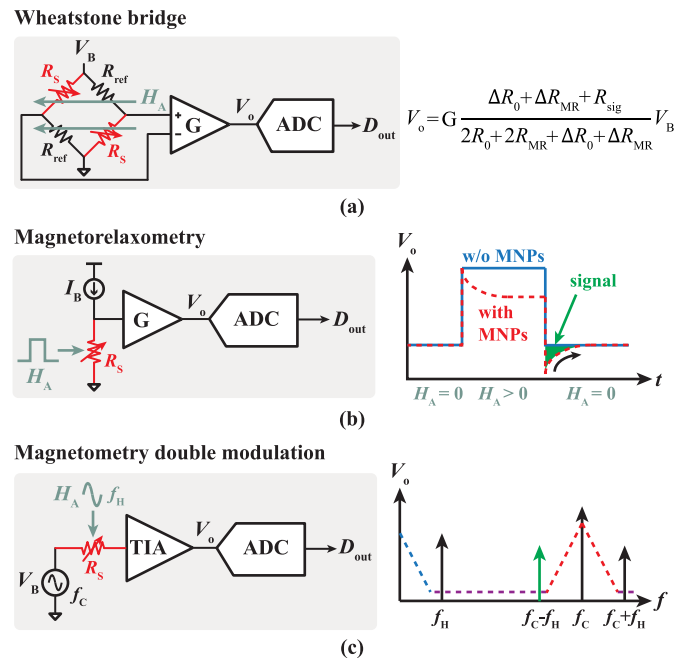


Fig. 3. Prior art magnetic biosensor AFEs: (a) Wheatstone bridge, (b) magnetorelaxometry, and (c) magnetometry with double modulation.

with sub-ppm sensitivity, an input-referred noise power spectral density (PSD) of $46.4 \text{ nT}/\sqrt{\text{Hz}}$, an input-referred baseline less than 0.235 mT , and a readout time of 11 ms . This work is an extended version of a previously published paper [39].

The rest of the paper is organized as follows: in Section II, prior art is briefly reviewed followed by the proposed system architecture in Section III. Section IV presents the circuit implementation with measurements results in Section V. Finally, conclusions are drawn in Section VI.

II. PRIOR ART

Several techniques have been proposed to resolve the large baseline-to-signal ratio issue discussed previously regarding GMR sensors. A Wheatstone bridge is the most commonly used technique, where two active sensors and two reference sensors form the bridge, as shown in Fig. 3(a) [40]–[42]. An instrumentation amplifier followed by an ADC captures the differential signal. This technique ideally eliminates all common-mode baseline signals (R_0 and R_{MR}) and the output is proportional to R_{sig} . However, sensor mismatch, ΔR_0 and ΔR_{MR} , eat into the dynamic range. Therefore, the gain, G , must be reduced by $(\Delta R_0 + \Delta R_{MR})/R_{sig}$ to accommodate the mismatch and thus decreases the resolution by $10^2 - 10^5 \times$ for a 10% mismatch.

Instead of directly measuring R_{sig} when H_A is applied, magnetorelaxometry measures the MNP's temporal relaxation response after removing the magnetic field, as shown in Fig. 3(b) [17], [18]. This approach eliminates the R_{MR} baseline and is immune to sensor mismatch when using magnetic correlated double sampling (CDS) [18], [43], [44]. However, the MNP relaxation timescale spans from ns to s for different sized MNPs

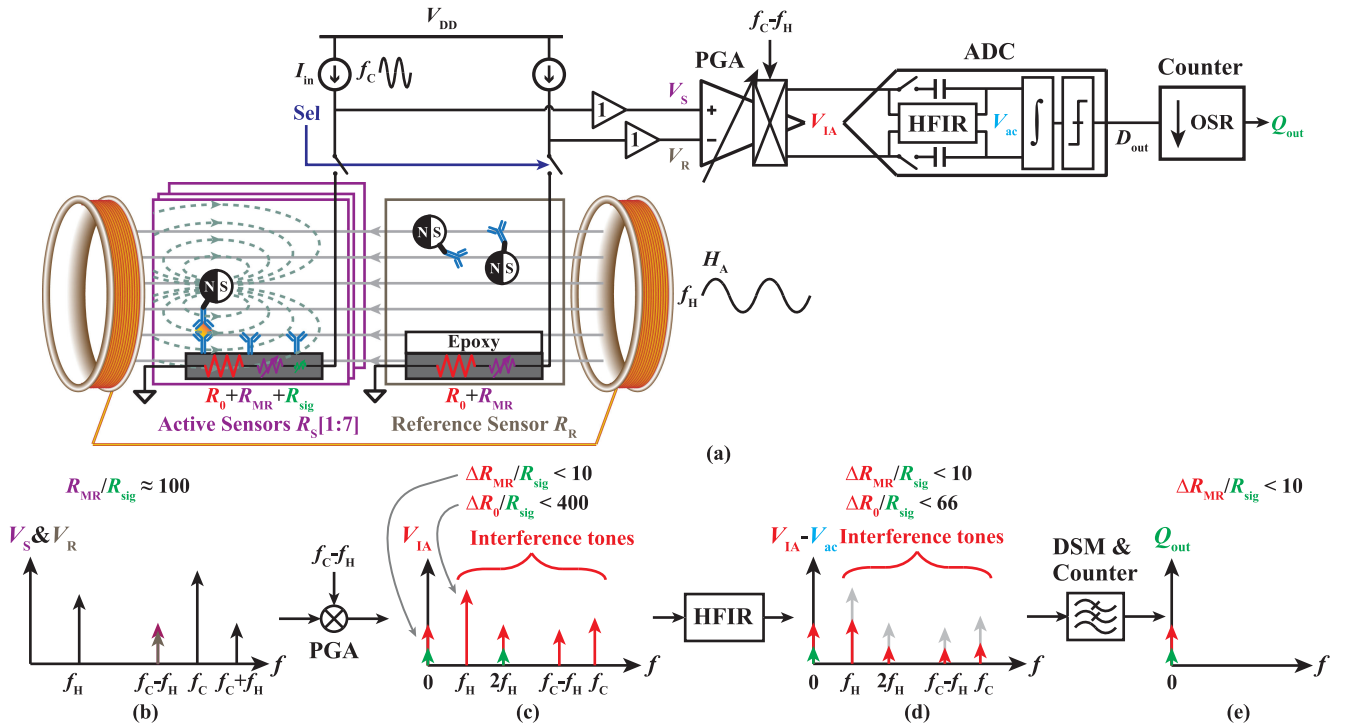


Fig. 4. (a) System architecture containing sensor bias, a PGA, and an ADC with a decimation filter. Illustration of spectrum at (b) V_S and V_R , (c) V_{IA} with and without sensor mismatch, (d) $V_{IA} - V_{ac}$ with and without HFIR sampling, and (e) Q_{out} .

[45]–[48]. Detecting slow relaxation signals integrates significant $1/f$ noise [43] whereas a high speed AFE and fast, pulsed magnetic field are required to detect fast relaxation signals [17], [18].

The magnetometry double modulation technique, shown in Fig. 3(c), applies an ac excitation (either a voltage or current) at frequency f_C and an ac magnetic field at frequency f_H to the sensor [20], [21]. This “double modulation” scheme spectrally separates the resistive (*i.e.* R_0 at f_C) and magnetoresistive components (*i.e.* R_{MR} and R_{sig} at $f_C \pm f_H$) of the signal. There are several benefits to this technique, namely the R_0 baseline can be reduced using excitation/carrier suppression [21], lock-in detection enables a very narrow noise bandwidth, and $1/f$ noise can be partially removed provided that f_H is at a higher frequency than the $1/f$ noise corner frequency. (Note that some of the $1/f$ noise is of magnetic origin and thus not mitigated by this technique.) However, the signal at $f_C \pm f_H$ still contains the R_{MR} baseline, which can be $100\times$ larger than R_{sig} . Moreover, the modulation scheme requires a higher bandwidth ADC and signal processing algorithms for demodulation.

III. SYSTEM ARCHITECTURE

We propose a new MR sensor front-end, as shown in Fig. 4(a), to improve tolerance of sensor mismatch and relax the DR requirement. The AFE contains three main blocks: sensor bias, a programmable gain amplifier (PGA) with gain G , and an ADC with a decimation filter and high-frequency interference rejection (HFIR) sampling. The AFE works as follows: A sinusoidal bias current, I_{in} , is applied to the selected active sensor,

R_S , and a reference sensor, R_R . Compared to using a voltage bias, current bias is spectrally purer and was thus chosen in this work [21]. Meanwhile, a sinusoidal magnetic field H_A generated from an off-chip Helmholtz coil is applied to both sensors. After buffering, the voltage at nodes V_S and V_R is

$$V_{S,R} = I_0 R_0 + I_0 R_{MR} \sin(2\pi f_H t) + \Delta I R_0 \sin(2\pi f_C t) + \left[\frac{\Delta I (R_{MR} + R_{sig})}{2} \right] \sin(2\pi (f_C \pm f_H) t) \quad (1)$$

where I_0 and ΔI are the dc and ac components of the bias current, respectively, R_0 is nominal resistance of the active and reference sensor, and R_{MR} is magnetoresistance of the active and reference sensor. It should be noted that the reference sensor is covered by an epoxy that prevents MNP binding, thus there is no R_{sig} detected by R_R . Furthermore, since R_R is on the same die with the sensor array ($R_S[1:7]$), it rejects common-mode environmental perturbations such as temperature drift removing the need for complicated temperature correction routines [49].

Spectrums at nodes V_S and V_R are illustrated in Fig. 4(b). Based on (1), although R_{sig} has been modulated away from R_0 through the double modulation scheme, R_{MR} is still at the same frequency as R_{sig} . With perfect matching between R_S and R_R (*i.e.* $R_{MR,s} = R_{MR,r}$ and $R_{0,s} = R_{0,r}$), the PGA eliminates both common-mode baseline signals, amplifies R_{sig} , and down-modulates the signal from $f_C - f_H$ to dc. As a result, the voltage at node V_{IA} is

$$V_{IA} = \frac{G\Delta I R_{sig}}{2} + \left(\frac{G\Delta I R_{sig}}{2} \right) \sin(2\pi 2f_H t). \quad (2)$$

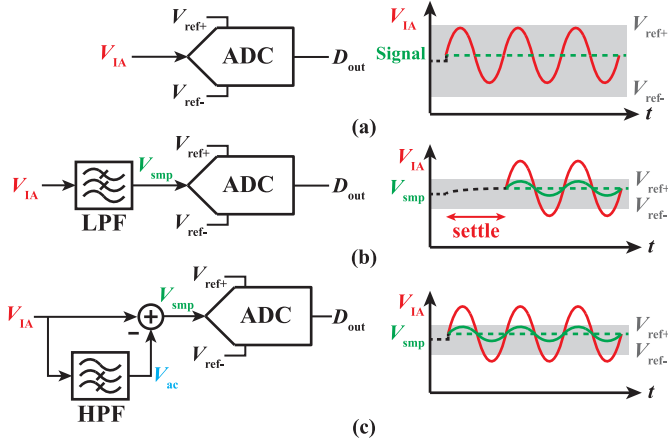


Fig. 5. (a) The ADC DR is limited by high frequency interference that can be reduced by (b) low-pass filtering or (c) high-pass feedforward filtering.

Although (2) indicates that high gain should be used to amplify the small signal, sensor mismatch limits it. Consider that R_S and R_R have R_0 mismatch where $\Delta R_0 = R_{0,s} - R_{0,r}$ and MR mismatch where $\Delta R_{MR} = R_{MR,s} - R_{MR,r}$. The voltage at node V_{IA} is

$$\begin{aligned}
 V_{IA} = G & \left[\frac{\Delta I (\Delta R_{MR} + R_{sig})}{2} + \Delta I \Delta R_0 \sin(2\pi f_H t) \right. \\
 & + \left. \left[\frac{\Delta I (\Delta R_{MR} + R_{sig})}{2} \right] \sin(2\pi 2f_H t) \right. \\
 & + I_0 \Delta R_0 \sin(2\pi (f_C - f_H) t) \\
 & \left. + I_0 \Delta R_{MR} \sin(2\pi f_C t) \right]. \quad (3)
 \end{aligned}$$

The spectrums with and without sensor mismatch are illustrated in Fig. 4(c), indicated as red and green arrows, respectively. It should be noted that transistor mismatch in the bias block is much smaller than the sensor mismatch and manifests similarly at the output whereas mismatch in the PGA and ADC are eliminated by chopping and correlated double sampling, respectively. Eq. (3) indicates that both ΔR_0 and ΔR_{MR} result in residual baselines at their respective frequencies. Although ΔR_{MR} results in a signal at the same frequency as R_{sig} , a 10% MR mismatch only leads to a baseline that is $\sim 10\times$ larger than the signal, which can be accommodated by increasing the ADC DR. However, a 10% R_0 mismatch causes a tone at f_H that can be $400\times$ larger than the signal, which would significantly increase the ADC DR requirement [Fig. 5(a)]. In theory, a low-pass filter (LPF) could be inserted between the PGA and ADC to filter out this interference [Fig. 5(b)] but would increase the settling time and thus the readout time, particularly when switching active sensors. Instead, a HFIR sampling scheme is proposed that reduces the ac interference without the settling penalty, as shown in Fig. 5(c). The feedforward sampling scheme is comprised of two phases. In the first phase, the high pass filter (HPF) passes all ac signals while blocking dc. In the second phase, the entire signal is sampled. After subtraction, V_{smp} contains only the

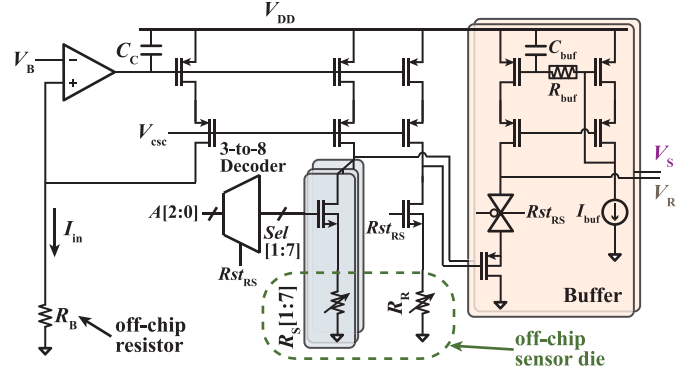


Fig. 6. Schematic of the sensor bias.

signal at dc. The transfer function of this filter is

$$H(s) = 1 - \frac{s}{s + \omega_p} = \frac{1}{1 + \frac{s}{\omega_p}} \quad (4)$$

where ω_p is the high-pass corner frequency. Eq. (4) shows that HPF feedforward technique has the same transfer function as a LPF, but comes with a $1,400\times$ reduction in the settling time.

This HFIR sampling technique embedded in the ADC sampler filters out these ac interference tones, and thus greatly relaxes the ADC DR requirement, as shown in Fig. 4(d). A first-order, incremental $\Delta\Sigma$ modulator (DSM) oversamples V_{IA} with an oversampling ratio (OSR) of 10,000. A subsequent counter decimates D_{out} , digitally filtering out all interference tones, leaving the desired signal at dc [Fig. 4(e)].

IV. CIRCUIT IMPLEMENTATION

A. Sensor Bias

The sensor bias block is composed of a bias current generator, sensor selection control logic, and two buffers (Fig. 6). The bias current generator uses an external reference voltage, V_B , an off-chip resistor, R_B , and an on-chip feedback loop to generate a bias current, $I_{in} = V_B / R_B$. A compensation capacitor, $C_C = 30$ pF, is added for stability. I_{in} is mirrored into two channels to bias the selected active sensor and reference sensor. The sensor in this work has a breakdown voltage of ~ 500 mV, which limits I_{in} . A 3-to-8 decoder generates control signals Sel [1:7] and a Rst_{RS} signal that opens all sensors during reset. Gated source followers that can also be disabled by Rst_{RS} buffer the voltages and drive the PGA. To reduce the noise mirrored from the bias current I_{buf} , the bias voltage is low-pass filtered by a pseudo-resistor R_{buf} and a capacitor C_{buf} .

B. Programmable Gain Amplifier

A 2-bit PGA rejects the large common-mode component of V_S and V_R while amplifying the differential signal. It is implemented by a capacitively-coupled instrumentation amplifier with chopper switches in the OTA and the feedback loop [Fig. 7(a)]. The choppers inside the OTA down-modulate the signal from $f_C - f_H$ to dc and up-modulate the offset and $1/f$ noise out-of-band where it is subsequently filtered. A 2-bit variable

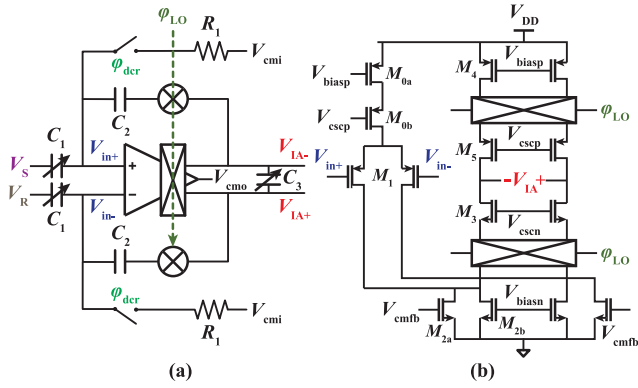


Fig. 7. Schematics of the (a) PGA and (b) fully-differential folded-cascode OTA with built-in down modulator.

capacitor, C_3 , is adjusted in tandem with the input capacitor C_1 to maintain the same closed-loop bandwidth across different gain modes. The OTA is implemented by a folded-cascode differential amplifier, as shown in Fig. 7(b). The choppers are placed at the cascode nodes for better settling and $M_{3,5}$ are large devices to reduce $1/f$ noise as their noise is not chopped. The tail current source is cascoded to improve the common-mode rejection ratio (CMRR) to be greater than 70 dB in simulation. To accommodate large common-mode input swing, the input dc voltage is set to 300 mV through a duty-cycled resistor (DCR), implemented by a switch controlled by ϕ_{dcr} and a poly-resistor R_1 . The output dc voltage is set to mid-supply by a switched-capacitor common-mode feedback network for large swing.

At the start of a measurement (*i.e.* Rst_{RS} goes from 0 \rightarrow 1), V_S and V_R are discharged from V_{DD} to V_{OP} , resulting in a rapid transient at V_{in} that needs time to settle back to V_{cmi} . The settling time would be prohibitively long as DCRs are usually designed to have very large impedances for low noise contribution. Worse, such settling happens every measurement when using time division multiplexing for multi-sensor readout, thus significantly increasing the overall readout time. To reduce the settling time due to sensor switching, a modified DCR timing scheme is proposed where the switches are briefly closed during and after sensor switching. Thus, V_{in} has a low-impedance path to V_{cmi} through R_1 enabling fast settling. Afterwards, the DCRs return to duty-cycled mode to operate as large bias resistors for low noise measurement. The timing diagram is shown in Fig. 8. Compared with a traditional DCR, the proposed fast-settling DCR reduces the settling time by 40%.

After settling, the PGA amplifies the signal with a programmable gain that depends on the sensor mismatch. Specifically, the PGA gain is set to amplify the dc signal as much as possible but ensure the ac swing is within the PGA linear range. An algorithm implemented on the FPGA determines which gain mode is appropriate for each sensor during startup.

C. Analog-to-Digital Converter

The ADC is implemented by a first-order incremental $\Delta\Sigma$ modulator, as shown in Fig. 9(a). The HFIR technique is embedded into the ADC sampling network. The HFIR block is

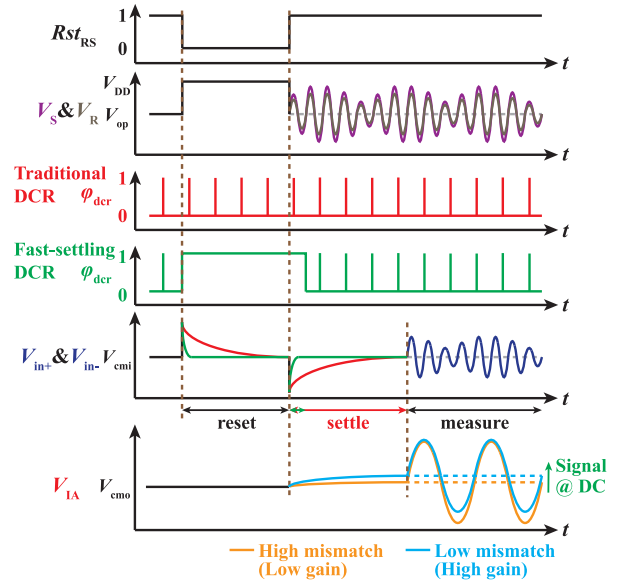


Fig. 8. PGA timing diagram that includes clocks and analog waveforms (ac swings not shown in the settling phase).

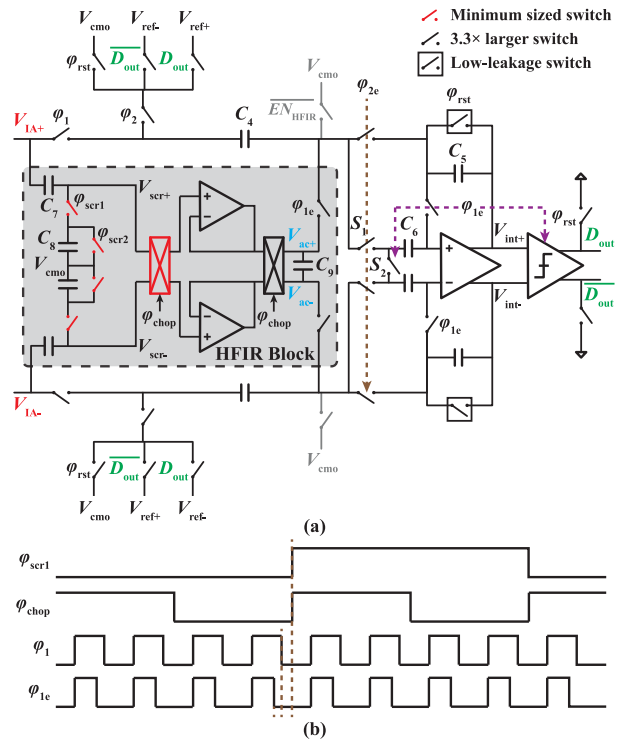


Fig. 9. ADC (a) schematic with HFIR sampling and (b) timing diagram.

implemented by a pseudo-differential, switched-capacitor HFPF followed by a chopped buffer. When the HFIR sampler is enabled ($EN_{HFIR} = 1$), the sampling capacitor, C_4 , samples the voltage difference (*i.e.* $V_{IA} - V_{ac}$) during the sampling phase ($\phi_{1,1e} = 1$). At the same time, C_6 samples the OTA offset and $1/f$ noise. It should be noted that the CDS realized by C_6 , S_1 , and S_2 is different from conventional CDS, which does not need

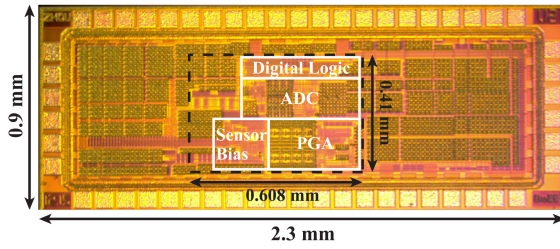


Fig. 10. Annotated die photo.

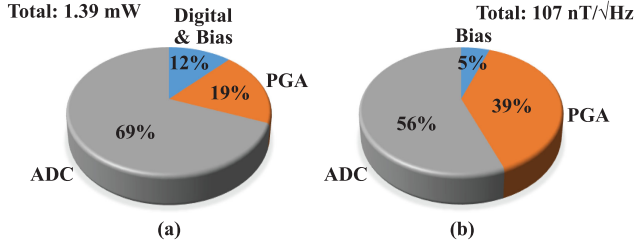


Fig. 11. Distribution of (a) power and (b) noise.

switches S_1 and S_2 to isolate the top plate of C_6 and V_{ac} . During the integration phase ($\varphi_{2,2e} = 1$), the charge stored on C_4 and C_6 is integrated on to C_5 . A dynamic comparator compares V_{int} to generate the digital output, D_{out} . The integrator is reset by two low-leakage switches, which provide negligible leakage (sub-fA) during normal operation [50].

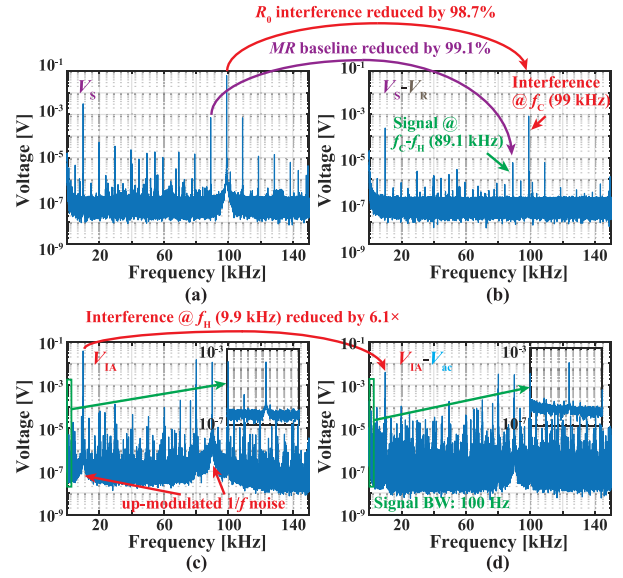
The timing diagram of the ADC is illustrated in Fig. 9(b). A non-overlapping clock generator creates φ_1 and φ_2 with early phases (φ_{1e} and φ_{2e}) to avoid signal-dependent charge injection. The chopping frequency, φ_{chop} , and the switched capacitor resistor (SCR) switching frequency, $\varphi_{scr1,2}$, are set to 1/4 and 1/8 of the sampling frequency, respectively. Both clocks change right after the sampling phase to ensure the maximum settling time.

To reject the ΔR_0 interference, the HFIR block must provide a low enough high-pass corner frequency, f_{HP} , yet must have a high enough low-pass corner frequency f_{LP} to ensure V_{ac} settles in time and does not integrate too much white noise. These two critical frequencies are

$$f_{HP} = \frac{f_{scr}C_8 + 2f_{chop}C_{in}}{2\pi C_7} \quad (5)$$

$$f_{LP} = \frac{1}{2\pi \left(\frac{1}{g_m} + R_{on} \right) 2C_9} \quad (6)$$

where f_{scr} is the SCR switching frequency, f_{chop} is the buffer chopping frequency, C_{in} is the capacitance at node V_{scr} , g_m is the buffer OTA transconductance, and R_{on} is the on-resistance of the output chopper. To have a low f_{HP} for better ac rejection, C_{in} must be minimized where C_{in} is mainly composed of the buffer input capacitance, switch parasitic capacitance, and interconnect parasitic capacitance. Since the buffer input transistors must be large enough to provide g_m for settling, C_{in} can only be reduced by decreasing the parasitic capacitance. Therefore, minimum sized switches are used in the SCR and the buffer input chopper,


 Fig. 12. Measured spectra at (a) V_S , (b) $V_S - V_R$, (c) V_{IA} , and (d) $V_{IA} - V_{ac}$.

indicated as red switches in Fig. 9(a). On the other hand, to ensure sufficient settling time, all other switches in the ADC are implemented by $3.3\times$ larger CMOS switches to reduce their on-resistance. The HPF in the HFIR is simulated to have a pass-band between 1.2 kHz and 20 MHz. The interference at 10 kHz passes through the HPF with -0.52 dB amplitude loss and 6.2° phase shift. Accordingly, after subtraction, the interference is reduced by $8.3\times$, thus relaxing the ADC DR requirement.

V. MEASUREMENT RESULTS

This chip was fabricated in a TSMC 180-nm CMOS process. An annotated die photo is shown in Fig. 10. It operates from a single supply of 1.8 V and consumes 1.39 mW excluding the sensor bias, which is dependent on the sensor resistance and consumes 5.4 mW for the $150\ \Omega$ sensors used in this work. The power and input-referred noise contributions of each block are shown in Fig. 11.

The proposed AFE was connected to a one-time use 8-pixel GMR sensor chip (MagArray, Inc.) placed inside of a custom designed Helmholtz coil. A 3D-printed chip holder forms a $100\ \mu\text{L}$ well over the sensing area. The sensors nominally have an R_0 of $150\ \Omega$ and a MR ratio of 9.04%. The synchronized excitation sources and clocks were generated externally by two function generators (Keysight 33600A) with $f_H = 9.9$ kHz, $f_C = 99$ kHz, and $f_C - f_H = 89.1$ kHz. A power amplifier (Kepco BOP 36-12) provides an ac current at f_H to the Helmholtz coil to generate an ac magnetic field of $60\ \text{Oe}_{pp}$ that was verified by a Gauss meter (LakeShore 475 DSP). It should be noted that the maximum f_H is 9.9 kHz, limited by the Helmholtz coil's large inductance ($\sim 80\ \mu\text{H}$). The digital inputs and outputs were controlled by an FPGA (Opal Kelly XEM6310).

Fig. 12 shows the measured spectra at critical nodes. In Fig 12(a), the sensor output (node V_S) contains large tones at f_H , f_C , and $f_C \pm f_H$. Most of the baselines are suppressed by the reference sensor, leaving only the residue tones due to

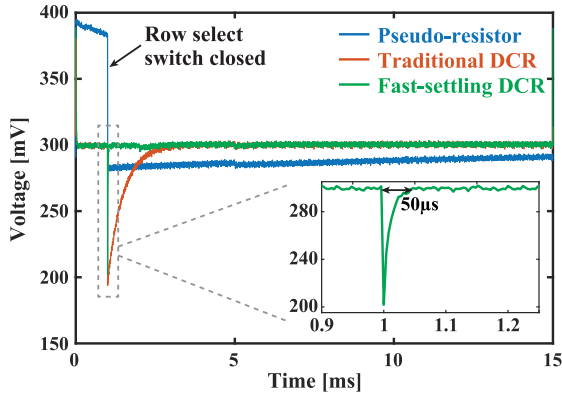


Fig. 13. Measured settling time of pseudo-resistor, DCR, and fast settling DCR.

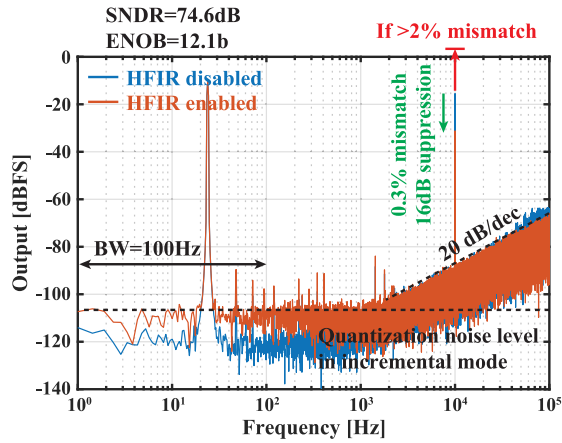


Fig. 14. Measured ADC spectra with and without HFIR sampling.

mismatch [Fig. 12(b)]. The PGA down-modulates the signal to dc, and up-modulates $1/f$ noise [Fig. 12(c)]. The HFIR sampling technique reduces the interference tone at f_H by $6.1\times$, as shown in Fig. 12(d). The suppression is slightly lower than in simulation due to larger parasitics at node V_{scr} .

Fig. 13 shows measured settling times of the PGA with a pseudo-resistor, a traditional DCR, and the proposed fast-settling DCR, all implemented on-chip for comparison. After the row select switch closed, a sudden ~ 100 mV voltage drop at V_{in} was observed. The pseudo-resistor, traditional DCR, and fast-settling DCR had a recovery time of >14 ms, ~ 2 ms, and ~ 50 μ s, respectively. Thus, the proposed fast-settling DCR achieves $40\times$ faster settling than a traditional DCR.

The ADC achieves 74.6 dB SNDR and an ENOB of 12.1 bits within a 100 Hz bandwidth, as shown in Fig. 14. Also evident from the spectra is the first-order noise shaping. The ADC was also measured with an in-band signal tone and an out-of-band interference tone at f_H . The amplitude of the interference tone was calculated based on 0.3% R_0 mismatch to avoid saturating the ADC when the HFIR is disabled. The spectra demonstrate 16-dB suppression of the interference tone by the HFIR sampling. Although the HFIR sampling increases the in-band noise, it is

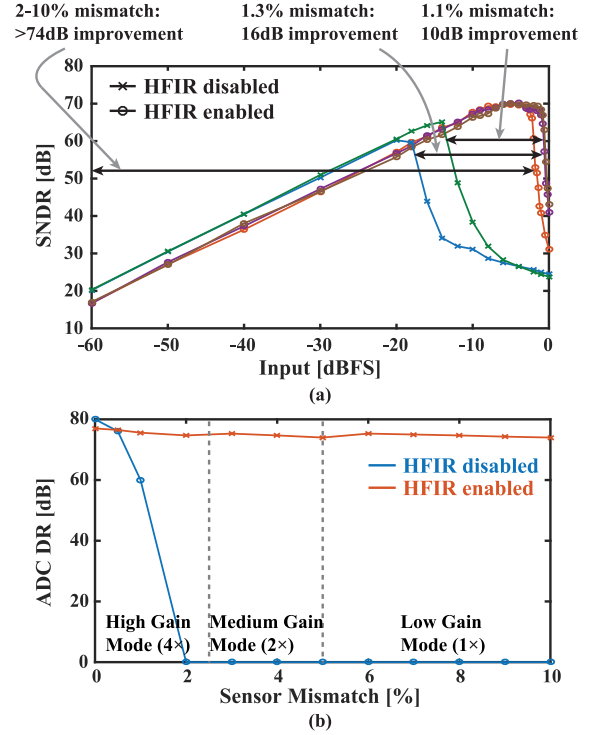


Fig. 15. (a) Measured ADC SNDR under different sensor mismatch conditions. (b) ADC DR vs. sensor mismatch.

still comparable to the ADC quantization noise in incremental mode (-106 dBFS).

The HFIR sampling improves the ADC DR by reducing the ac swing from ΔR_0 . In Fig. 15(a), the ADC DR is improved by 10, 16, and >74 dB for 1.1%, 1.3%, and 2-10% mismatch, respectively. Fig 15(b) plots the ADC DR versus sensor mismatch. When the mismatch is $<0.5\%$, the ADC DR is higher without the HFIR sampling since the ac swing from mismatch is smaller than the added noise. However, when the mismatch is $>0.5\%$, the HFIR sampling benefits the ADC by canceling the interference. When the mismatch is $>2\%$, the ADC is saturated by the interference tone if the HFIR sampling is disabled.

The readout time can be as fast as 11 ms (1 ms reset + settling and 10 ms measuring), but it can also be traded off for higher sensitivity by averaging. Fig. 16(a) shows the sensitivity versus readout time for different PGA gains. The spectra for the fastest readout and highest sensitivity are plotted in Fig. 16(b) and (c), respectively. In the fastest readout mode, it takes 11 ms per acquisition and integrates 464 nT_{RMS} noise in high gain mode, which corresponds to a 4.4 ppm sensitivity and a theoretical limit of detection (LOD) of 9,280 MNPs ($d = 50$ nm). In contrast, the highest sensitivity mode takes 880 ms per acquisition but integrates only 111 nT_{RMS} noise corresponding to a sensitivity of 0.98 ppm and a theoretical LOD of 2,200 MNPs. Further increasing the acquisition time would not improve the sensitivity since the noise is limited by the $1/f$ noise and cannot be reduced by averaging.

Temperature sensitivity measurements are shown in Fig. 17. To measure the temperature sensitivity, a low temperature coefficient resistor with similar resistance as R_0 replaced the reference

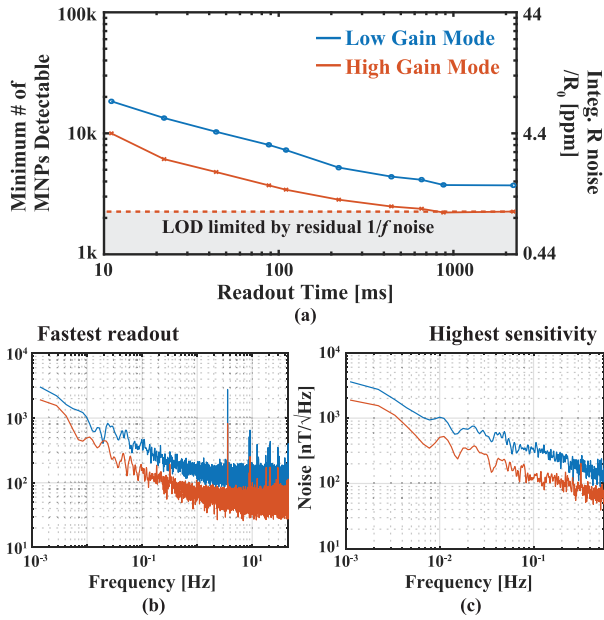


Fig. 16. (a) Measured integrated noise vs. readout time for different gain modes. Measured input-referred noise spectra for (b) fastest readout (11 ms) and (c) highest sensitivity (880 ms).

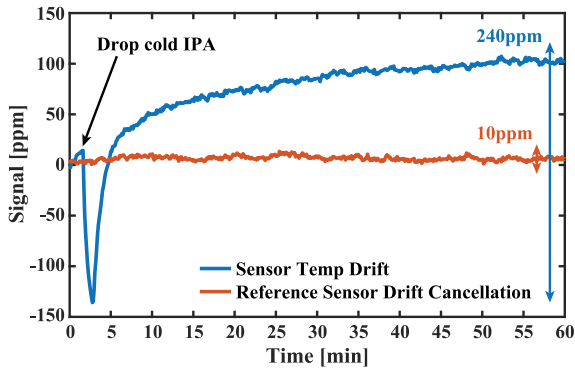


Fig. 17. Measured temperature drift.

sensor such that the reference sensor would not cancel the temperature change. Cold isopropyl alcohol (IPA) at 4 °C was dropped on sensor surface at $t = 2$ min, which caused a large temperature-induced signal (~ 240 ppm). The same experiment performed with the reference sensor caused only a negligible signal (10 ppm) demonstrating the ability to reject environmental common-mode interference.

Biological experiments were conducted to validate the system performance. Sensors were functionalized with biotinylated-bovine serum albumin (Biotin-BSA) for use as a positive control, a captured antibody for human Interleukin 6 (IL-6), a cancer biomarker, and BSA for use as a negative control to monitor non-specific binding. The reference sensor was covered by epoxy, preventing it from sensing signal from the MNPs. To functionalize the sensor surface with the BSA or IL-6 antibodies, chips were washed with acetone, methanol, and IPA. After 5 minutes of cleaning with oxygen plasma, 1% Poly(allylamine) in distilled water (DIW) was added for another 5 minutes. After baking for 1 hour at 110 °C, 2% aqueous Poly(ethylene-alt-maleic

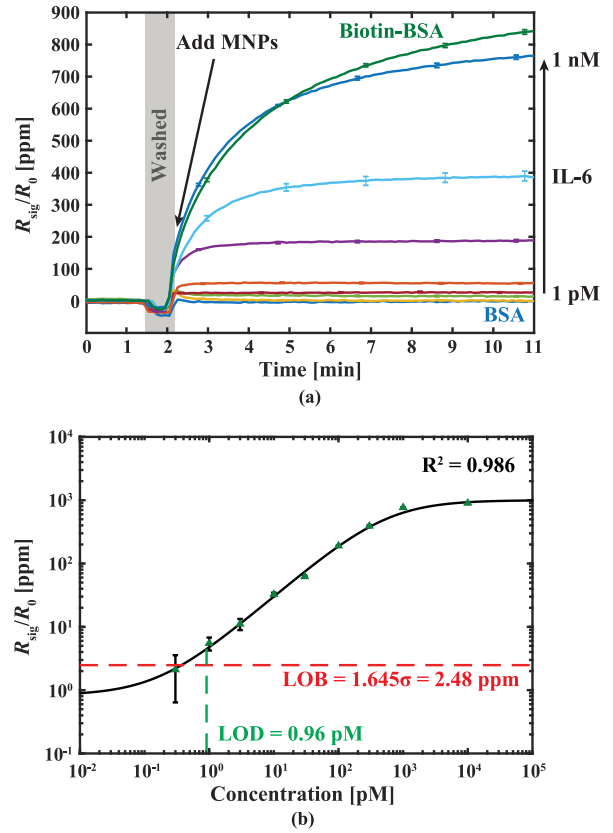


Fig. 18. (a) Measured binding curves for negative control (BSA), positive control (Biotin-BSA), and IL-6 at different concentrations; (b) IL-6 calibration curve.

anhydride) in DIW was added to the chips for 5 minutes. Finally, the chips were baked for 1 hour at 160 °C. Capture reagents were spotted on the sensors and incubated at 4 °C overnight.

Fig. 18(a) shows overlaid transient measurement results for the negative control, positive control, and various concentrations of IL-6. In each assay, the sensors were washed with phosphate buffered saline (PBS) 1 minute after starting and MNPs (Streptavidin microbeads, catalog number #130-048-101, Miltenyi Biotec) were added afterwards. The system continuously measured the real-time binding curves in the high gain mode. After the binding curves saturated, a washing step (not shown in Fig. 18(a)) was performed to remove any non-specific binding. Multiple experiments showed that the signal after washing did not drop indicating that the binding was highly specific. The averages of each measurement ($n = 6$ sensors) are compiled to obtain the calibration curve shown in Fig. 18(b). The resulting data is fit with a 4-parameter logistical (4-PL) regression with an R^2 value of 0.986. The LOD, calculated based on [51], is 0.96 pM.

This work is summarized in Table I and compared to state-of-the-art magnetic sensor AFEs. Compared with other magnetometry-based designs such as Wheatstone bridge and conventional double modulation architectures, this work presents HFIR sampling technique and fast settling DCR to break the baseline rejection limit from sensor mismatch and reduce system settling time, respectively. As a result, this work achieves $22.7\times$ faster readout time, $>7.8\times$ lower input-referred

TABLE I
COMPARISON WITH THE CURRENT STATE-OF-THE-ART MAGNETIC SENSOR AFEs

	H. Wang ISSCC 2009 [16]	S. Gambini JSSC 2013 [18]	T. Costa TBioCAS 2017 [19]	S.J. Han ISSCC 2007 [20]	D.A. Hall JSSC 2013 [21]	This work
Sensor Type	LC	Hall	GMR	GMR	GMR	GMR
Sensor Resistance (k Ω)	N/A	N/A	0.85	N/A	1.92	0.15
MR Ratio (%)	N/A	N/A	5.37	N/A	9.2	9.04
MNP Size (nm)	1,000	1,000	250	50	50	50
Technology Node (μ m)	0.13	0.18	0.35	0.25	0.18	0.18
AFE Architecture	LC oscillator	V/I Converter	Amplifier	Mixer + PGA	TIA	PGA with Mixer
ADC Architecture	VCO-based	Inc. $\Delta\Sigma$	No ADC	No ADC	$\Delta\Sigma$	Inc. $\Delta\Sigma$ with HFIR
Input-referred Noise (nT/ \sqrt Hz)	N/A	270	11.5 ^ψ	N/A	49	107.1 (low gain) 46.4 (high gain)
Sensor Mismatch Tolerance	N/A	N/A	N/A	N/A	N/A	10% (low gain) 2.5% (high gain)
Power/Ch. (mW)*	N/A	0.825	4.9 ^ψ	N/A	3.15	1.39
Area/Ch. (mm ²)	N/A	0.012	3.17	N/A	0.219	0.249
Input-referred Baseline (mT)	N/A	0.007	1.84	N/A	7.09	< 0.235
Readout Time/Ch. (ms)	400 [†]	50	1,000	250	250	11
Temperature Correction	Yes	No	No	Yes	Yes	Yes

*Does not include sensor bias and magnetic field generator. ^ψ Does not include power and noise from ADC. [†] Read from figures.

baseline, and $2.3\times$ lower power. Although relaxometry-based designs inherently eliminate the baseline, their lower signal amplitude and higher input-referred noise confound high sensitivity measurements. Most importantly, this design can tolerate up to 10% sensor mismatch making it compatible with commercial tolerances for MR sensor fabrication.

VI. CONCLUSION

In this paper, we present a GMR sensor front-end and an ADC for magnetic biosensing. The design uses a reference sensor to cancel most of the baseline signals and reject common-mode interference, such as temperature drift. A fast-settling DCR is presented to improve the system settling time by $40\times$ comparing to a traditional DCR enabling fast readout. A HFIR sampling technique is embedded into the ADC to reject high frequency interference from sensor mismatch, thus improving the ADC equivalent DR to tolerate high sensor mismatch. As a result, the proposed AFE achieves sub-ppm sensitivity, fast readout time of 11 ms, and tolerance to sensor mismatch up to 10%. It makes this work ideal for multichannel, high sensitivity, PoC diagnostic systems.

REFERENCES

- [1] S. K. Vashist, "Point-of-care diagnostics: Recent advances and trends," *Biosensors*, vol. 7, no. 4, Dec. 2017, Art. no. 62.
- [2] S. Nayak, N. R. Blumenfeld, T. Laksanasopin, and S. K. Sia, "Point-of-care diagnostics: Recent developments in a connected age," *Analytical Chem.*, vol. 89, no. 1, pp. 102–123, Jan. 2017.
- [3] S. K. Vashist, P. B. Lupta, L. Y. Yeo, A. Ozcan, and J. H. T. Luong, "Emerging technologies for next-generation point-of-care testing," *Trends Biotechnol.*, vol. 33, no. 11, pp. 692–705, Nov. 2015.
- [4] "Point-of-care diagnostics market analysis by testing, platform, mode, end-user-global forecast to 2022: MarketsandMarkets," Oct. 2019. [Online]. Available: <https://www.marketsandmarkets.com/Market-Reports/point-of-care-diagnostic-market-106829185.html>
- [5] A. C. Sun and D. A. Hall, "Point-of-care smartphone-based electrochemical Biosensing," *Electroanalysis*, vol. 31, no. 1, pp. 2–16, 2019.
- [6] H. Liu *et al.*, "A wash-free homogeneous colorimetric immunoassay method," *Theranostics*, vol. 6, no. 1, pp. 54–64, Jan. 2016.
- [7] Y. Xiang and Y. Lu, "Using personal glucose meters and functional DNA sensors to quantify a variety of analytical targets," *Nature Chem.*, vol. 3, no. 9, pp. 697–703, Jul. 2011.
- [8] M. Sánchez-Carbayo, M. Mauri, R. Alfayate, C. Miralles, and F. Soria, "Analytical and clinical evaluation of TSH and thyroid hormones by electrochemiluminescent immunoassays," *Clin. Biochem.*, vol. 32, no. 6, pp. 395–403, Aug. 1999.
- [9] A. Thiha and F. Ibrahim, "A colorimetric enzyme-linked immunosorbent assay (ELISA) detection platform for a point-of-care dengue detection system on a lab-on-compact-disc," *Sensors*, vol. 15, no. 5, pp. 11431–11441, May 2015.
- [10] V. Borse and R. Srivastava, "Fluorescence lateral flow immunoassay based point-of-care nanodiagnosics for orthopedic implant-associated infection," *Sensors Actuators B Chem.*, vol. 280, pp. 24–33, Feb. 2019.
- [11] D.-S. Wang and S.-K. Fan, "Microfluidic surface plasmon resonance sensors: From principles to point-of-care applications," *Sensors*, vol. 16, no. 8, Jul. 2016, Art. no. 1175.
- [12] J. D. Newman and A. P. F. Turner, "Home blood glucose biosensors: a commercial perspective," *Biosens. Bioelectron.*, vol. 20, no. 12, pp. 2435–2453, Jun. 2005.
- [13] D. Issadore *et al.*, "Ultrasensitive clinical enumeration of rare cells ex vivo using a μ -Hall detector," *Sci. Translational Med.*, vol. 4, no. 141, Jul. 2012, Art. no. 141ra92.
- [14] K. Lei, H. Heidari, P. Mak, M. Law, F. Maloberti, and R. P. Martins, "28.1 A handheld 50pM-sensitivity micro-NMR CMOS platform with B-field stabilization for multi-type biological/chemical assays," in *Proc. IEEE Int. Solid State Circuits Conf.*, 2016, pp. 474–475.
- [15] N. Sun, T. Yoon, H. Lee, W. Andress, R. Weissleder, and D. Ham, "Palm NMR and 1-chip NMR," *IEEE J. Solid-State Circuits*, vol. 46, no. 1, pp. 342–352, Jan. 2011.
- [16] H. Wang, Y. Chen, A. Hassibi, A. Scherer, and A. Hajimiri, "A frequency-shift CMOS magnetic biosensor array with single-bead sensitivity and no external magnet," in *Proc. IEEE Int. Solid State Circuits Conf. Dig. Tech. Papers*, 2009, pp. 438–439.
- [17] P. P. Liu *et al.*, "Magnetic relaxation detector for microbead labels," *IEEE J. Solid-State Circuits*, vol. 47, no. 4, pp. 1056–1064, Apr. 2012.
- [18] S. Gambini, K. Skucha, P. P. Liu, J. Kim, and R. Krigel, "A 10 kPixel CMOS hall sensor array with baseline suppression and parallel readout for immunoassays," *IEEE J. Solid-State Circuits*, vol. 48, no. 1, pp. 302–317, Jan. 2013.
- [19] T. Costa, F. A. Cardoso, J. Germano, P. P. Freitas, and M. S. Piedade, "A CMOS front-end with integrated magnetoresistive sensors for biomolecular recognition detection applications," *IEEE Trans. Biomed. Circuits Syst.*, vol. 11, no. 5, pp. 988–1000, Oct. 2017.
- [20] S. J. Han, H. Yu, B. Murmann, N. Pourmand, and S. X. Wang, "A high-density magnetoresistive biosensor array with drift-compensation mechanism," in *Proc. IEEE Int. Solid State Circuits Conf. Dig. Tech. Papers*, 2007, pp. 168–169.
- [21] D. A. Hall, R. S. Gaster, K. A. A. Makinwa, S. X. Wang, and B. Murmann, "A 256 Pixel Magnetoresistive biosensor microarray in 0.18 μ m CMOS," *IEEE J. Solid-State Circuits*, vol. 48, no. 5, pp. 1290–1301, May 2013.

- [22] R. S. Gaster *et al.*, "Matrix-insensitive protein assays push the limits of biosensors in medicine," *Nature Med.*, vol. 15, no. 11, pp. 1327–1332, Nov. 2009.
- [23] X. Zhou, C.-C. Huang, and D. A. Hall, "Magnetoresistive biosensors for quantitative proteomics," *Proc. SPIE*, vol. 10352, Aug. 2017, Art. no. 103520F.
- [24] J. E. Aubin, "Autofluorescence of viable cultured mammalian cells," *J. Histochem. Cytochem. Off. J. Histochem. Soc.*, vol. 27, no. 1, pp. 36–43, Jan. 1979.
- [25] H. Giloh and J. W. Sedat, "Fluorescence microscopy: Reduced photobleaching of rhodamine and fluorescein protein conjugates by n-propyl gallate," *Science*, vol. 217, no. 4566, pp. 1252–1255, Sep. 1982.
- [26] J. S. Swensen *et al.*, "Continuous, real-time monitoring of cocaine in undiluted blood serum via a microfluidic, electrochemical aptamer-based sensor," *J. Amer. Chem. Soc.*, vol. 131, no. 12, pp. 4262–4266, Apr. 2009.
- [27] R. S. Gaster *et al.*, "Quantification of protein interactions and solution transport using high-density GMR sensor arrays," *Nature Nanotechnol.*, vol. 6, no. 5, pp. 314–320, May 2011.
- [28] R. S. Gaster, D. A. Hall, and S. X. Wang, "nanoLAB: An ultraportable, handheld diagnostic laboratory for global health," *Lab Chip*, vol. 11, no. 5, pp. 950–956, Mar. 2011.
- [29] D. Kim *et al.*, "Nanosensor dosimetry of mouse blood proteins after exposure to ionizing radiation," *Sci. Rep.*, vol. 3, Jul. 2013, Art. no. 2234.
- [30] H. Yu, S. J. Osterfeld, L. Xu, R. L. White, N. Pourmand, and S. X. Wang, "Giant magnetoresistive biosensors for molecular diagnosis: Surface chemistry and assay development," *Proc. SPIE*, vol. 7035, Aug. 2008, Art. no. 70350E.
- [31] Z. Q. Lei *et al.*, "Liver cancer immunoassay with magnetic nanoparticles and MgO-based magnetic tunnel junction sensors," *J. Appl. Phys.*, vol. 111, no. 7, Mar. 2012, Art. no. 07E505.
- [32] P. P. Freitas, R. Ferreira, S. Cardoso, and F. Cardoso, "Magnetoresistive sensors," *J. Phys. Condens. Matter*, vol. 19, no. 16, Apr. 2007, Art. no. 165221.
- [33] E. Y. Tsymlal and I. Zutic, *Handbook of Spin Transport and Magnetism*. Hoboken, NJ, USA: CRC Press, 2011.
- [34] D. A. Hall *et al.*, "GMR biosensor arrays: A system perspective," *Biosens. Bioelectron.*, vol. 25, no. 9, pp. 2051–2057, May 2010.
- [35] D. Mazumdar, X. Liu, B. D. Schrag, W. Shen, M. Carter, and G. Xiao, "Thermal stability, sensitivity, and noise characteristics of MgO-based magnetic tunnel junctions (invited)," *J. Appl. Phys.*, vol. 101, no. 9, Apr. 2007, Art. no. 09B502.
- [36] J. M. Teixeira *et al.*, "The effect of pinhole formation/growth on the tunnel magnetoresistance of MgO-based magnetic tunnel junctions," *J. Appl. Phys.*, vol. 106, no. 7, Oct. 2009, Art. no. 073707.
- [37] O. Y. Galkin, O. B. Besarab, M. O. Pysmenna, Y. V. Gorshunov, and O. M. Dugan, "Modern magnetic immunoassay: Biophysical and biochemical aspects," *Regulatory Mechanism Biosyst.*, vol. 9, no. 1, pp. 47–55, 2018.
- [38] C. Reig, D. Ramírez, F. Silva, J. Bernardo, and P. Freitas, "Design, fabrication, and analysis of a spin-valve based current sensor," *Sensors Actuators Phys.*, vol. 115, no. 2, pp. 259–266, Sep. 2004.
- [39] X. Zhou, M. Sveiven, and D. A. Hall, "11.4 A fast-readout mismatch-insensitive magnetoresistive biosensor front-end achieving Sub-ppm sensitivity," in *Proc. IEEE Int. Solid State Circuits Conf.*, 2019, pp. 196–198.
- [40] J. C. Rife, M. M. Miller, P. E. Sheehan, C. R. Tamanaha, M. Tondra, and L. J. Whitman, "Design and performance of GMR sensors for the detection of magnetic microbeads in biosensors," *Sensors Actuators Phys.*, vol. 107, no. 3, pp. 209–218, Nov. 2003.
- [41] C.-P. Lee, M.-F. Lai, H.-T. Huang, C.-W. Lin, and Z.-H. Wei, "Wheatstone bridge giant-magnetoresistance based cell counter," *Biosens. Bioelectron.*, vol. 57, pp. 48–53, Jul. 2014.
- [42] M. F. Hansen and G. Rizzi, "Exchange-biased AMR bridges for magnetic field sensing and biosensing," *IEEE Trans. Magn.*, vol. 53, no. 4, pp. 1–11, Apr. 2017.
- [43] X. Zhou, C. Huang, and D. A. Hall, "Giant magnetoresistive biosensor array for detecting Magnetorelaxation," *IEEE Trans. Biomed. Circuits Syst.*, vol. 11, no. 4, pp. 755–764, Aug. 2017.
- [44] K. Kim *et al.*, "Magnetoresistive biosensors with on-chip pulsed excitation and magnetic correlated double sampling," *Sci. Rep.*, vol. 8, no. 1, Nov. 2018, Art. no. 16493.
- [45] N. L. Adolphi *et al.*, "Characterization of magnetite nanoparticles for SQUID-relaxometry and magnetic needle biopsy," *J. Magnetism Magn. Mater.*, vol. 321, no. 10, pp. 1459–1464, May 2009.
- [46] F. Wiekhorst, U. Steinhoff, D. Eberbeck, and L. Trahms, "Magnetorelaxometry assisting biomedical applications of magnetic nanoparticles," *Pharmaceutical Res.*, vol. 29, no. 5, pp. 1189–1202, May 2012.
- [47] C.-C. Huang, X. Zhou, and D. A. Hall, "Giant magnetoresistive biosensors for time-domain magnetorelaxometry: A theoretical investigation and progress toward an immunoassay," *Sci. Rep.*, vol. 7, Apr. 2017, Art. no. 45493.
- [48] F. W. Østerberg, G. Rizzi, and M. F. Hansen, "On-chip Brownian relaxation measurements of magnetic nanobeads in the time domain," *J. Appl. Phys.*, vol. 113, no. 23, Jun. 2013, Art. no. 234508.
- [49] D. A. Hall, R. S. Gaster, S. J. Osterfeld, B. Murmann, and S. X. Wang, "GMR biosensor arrays: Correction techniques for reproducibility and enhanced sensitivity," *Biosens. Bioelectron.*, vol. 25, no. 9, pp. 2177–2181, May 2010.
- [50] A. C. Sun, E. Alvarez-Fontecilla, A. G. Venkatesh, E. Aronoff-Spencer, and D. A. Hall, "High-density redox amplified coulometric discharge-based biosensor array," *IEEE J. Solid-State Circuits*, vol. 53, no. 7, pp. 2054–2064, Jul. 2018.
- [51] D. A. Armbruster and T. Pry, "Limit of blank, limit of detection and limit of quantitation," *Clin. Biochem. Rev.*, vol. 29, no. Suppl 1, pp. S49–S52, Aug. 2008.



Xiahan Zhou received the B.S. degree in microelectronics technology from the University of Electronic Science and Technology of China, Chengdu, China, in 2012, and the M.S. degree (Hons.) in electrical engineering from the University of Southern California, Los Angeles, CA, USA, in 2014. He is currently working toward the Ph.D. degree in electrical and computer engineering with University of California, San Diego, La Jolla, CA, USA.

His research interests are analog and mixed-signal circuits and systems for biosensors and medical devices. He received Qualcomm FMA fellowship award at 2017.



Michael Sveiven received the B.S. degree in biomedical engineering from the University of Arizona, Tucson, AZ, USA, in 2017.

He is currently working on point-of-care diagnostics for proteolytic diseases. He is currently optimizing surface chemistry techniques on magnetoresistive sensors to detect the presence of specific proteases often found in patients with Cystic Fibrosis, the most common, inherited fatal disease in Caucasians. His research focuses on the development of a point-of-care diagnostic device for rapid detection of proteases.



Drew A. Hall (S'07–M'12–SM'19) received the B.S. degree in computer engineering (Hons.) from the University of Nevada, Las Vegas, NV, USA, in 2005, and the M.S. and Ph.D. degrees in electrical engineering from Stanford University, Stanford, CA, USA, in 2008 and 2012, respectively.

From 2011 to 2013, he worked as a Research Scientist with the Intel Corporation in the Integrated Biosensors Laboratory. Since 2013, he has been with the University of California San Diego, where he is currently an Associate Professor with the Department of Electrical and Computer Engineering and an Affiliate Professor in the Department of Bioengineering. His research interests include bioelectronics, biosensors, analog circuit design, medical electronics, and sensor interfaces.

He was the co-recipient of the First Place in the Inaugural International IEEE Change the World Competition and First Place in the BME-IDEA Invention Competition, in 2009. He was the recipient of the Analog Devices Outstanding Designer Award in 2011, an Undergraduate Teaching Award in 2014, the Hellman Fellowship Award in 2014, an NSF CAREER Award in 2015, NIH Trailbalzer Award in 2019, and the Best Poster Award at BioCAS 2019. He is also a Tau Beta Pi Fellow.